Nanoscale

PAPER

View Article Online
View Journal

Open Access Article. Published on 10 July 2025. Downloaded on 8/5/2025 7:55:36 PM.
This article is licensed under a Creative Commons Attribution 3.0 Unported Licence.

Check for updates

Cite this: DOI: 10.1039/d5nr01575h

Modulation excitation pair distribution function experiments in catalysis to increase phase sensitivity†

Fabio Manzoni, *[a] Ansgar Meise [b] and Mirijam Zobel *[a]

Received 17th April 2025,
Accepted 8th July 2025

DOI: 10.1039/d5nr01575h

rsc.li/nanoscale

Heterogeneous catalysts are often undergoing subtle structural changes in both the nanoparticles and the support phase under operating conditions. Catalytic cycling in *in situ* experiments between catalysis and dropout conditions allows for exploiting the power of modulation excitation (ME) experiments. While phase-sensitive detection (PSD) of ME experiments has been showcased for infrared and X-ray absorption spectroscopy in the past, here we present its first application to pair distribution function (PDF) analysis. We have performed *in situ* X-ray total scattering studies on two alumina-supported nickel (Ni@alumina) catalysts under methanation and hydrogen dropout conditions and showcased how PSD analysis of the modulation excitation pair distribution function (ME-PDF) data improves the signal-to-noise ratio in the phase-resolved PDF data, enabling us to detect otherwise hidden structural changes. We identify a metal–support interaction of the Ni nanoparticles with the γ-Al_2O_3 support when choosing the deposition–precipitation method for catalyst preparation. By way of contrast, an industrial catalyst with comparable catalytic performance and nanoparticle diameter showed dynamic surface oxidation of Ni nanoparticles during unstable H_2 supply.

1. Introduction

Identifying subtle structural changes that occur on the surface of nanoparticle (NP)-based catalysts during reaction conditions is still a considerable challenge in the field of heterogeneous catalysis.[1] Catalytically active NPs can interact with adsorbed and reactive gas molecules as well as with the support. Both interactions are accompanied by surface reconstruction processes, impacting bond distances, bond angles, and possibly even modifying NP shape and faceting.[2] These structural changes vary with the gas atmosphere composition and can be of transient, reversible or irreversible nature, with the latter resulting in catalyst degradation.[3–5] Furthermore, the support structure can also be affected by structural changes, forming interfacial phases at the support surface or contributing to strong metal support interaction phenomena.[6,7] Therefore, a deep structural understanding of both the NPs and support involved in the reaction is crucial in order to understand the final properties of the catalyst.[8–11] Experimental techniques are required, which allow us to probe the catalyst structure under *in situ* and *operando* conditions with high sensitivity for such insight.

Among the different catalysts for CO_2 methanation, Ni-based materials are the most widely used for industrial applications due to their high conversion and selectivity towards methane, being a non-critical raw material too. From an industrial point of view, Ni@γ-Al_2O_3 catalysts are the most important systems because of the high longevity of alumina supports. However, several open questions remain regarding the role of the support surface in the catalytic activity and the structural changes of the NPs (surface reconstruction and interfacial oxide formation) during catalysis.[12] Moreover, with the transition from fossil to renewable energies, unsteady supply of feedstock or energy needs to be considered when planning industrial processes and designing catalysts.[11] Fluctuations in operation conditions can provoke structural changes, for instance, due to surface redox reactions,[13] and the occurrence of transient interfacial structures due to surface reconstruction processes.[2] For the methanation process converting renewable H_2 with CO_2 to water and methane, *in situ* studies can readily address an unsteady H_2 supply by switching in experiments between catalysis conditions and hydrogen-poor or hydrogen-free dropout conditions. Different techniques have been gaining attention in recent years to measure these dynamic changes. Structure-sensitive techniques such as powder X-ray

[a]Institute of Crystallography, RWTH Aachen University, 52066 Aachen, Germany. E-mail: manzoni@ifk.rwth-aachen.de, zobel@ifk.rwth-aachen.de
[b]Ernst Ruska-Centre for Microscopy and Spectroscopy with Electrons, Forschungszentrum Jülich GmbH, 52428 Jülich, Germany

† Electronic supplementary information (ESI) available. See DOI: https://doi.org/10.1039/d5nr01575h

Open Access Article. Published on 10 July 2025. Downloaded on 8/5/2025 7:55:36 PM.
This article is licensed under a Creative Commons Attribution 3.0 Unported Licence.

diffraction (PXRD),[14] X-ray absorption spectroscopy (XAS)[15] or X-ray total scattering with pair distribution function (PDF)[16,17] analysis are able to provide detailed structural insight into the sample with sub-second resolution at modern synchrotron facilities.[18]

Among all these techniques, the PDF is important for studying disordered and nanostructured materials yielding information about the short-range order and, in the case of NPs, their average size. The PDF is a histogram of interatomic distances in the sample and is accessed by Fourier transformation of PXRD data over a wide angular range; see ref. 19 for an introduction to the PDF technique for disordered materials.

The challenge in refining the experimental PDF data of heterogeneous catalysts is to properly account for subtle structural changes of the NPs or restructuring of the catalyst support. If the support does not restructure, difference PDFs (d-PDFs) can be calculated by subtracting the scattering contribution of the unloaded support, thus leaving the experimental PDF of the NPs only.[20] If the support restructures but still allows for an adequate d-PDF calculation, one may achieve additional insight into the support restructuring from the d-PDF. This was, for example, shown for distortions of the MOF NU-1000 framework.[21] Such d-PDF calculations can also be applied to PDFs calculated from neutron[22] or electron diffraction data.[23] In order to track co-existing species during the catalytic reaction, such as spectator and active species, non-negative matrix factorization (NMF)[24] and principal component analysis (PCA)[25] have been applied. Using these mathematical approaches, it is possible to extract information from individual components of a multi-component system and analyse them individually. For example, Geddes *et al.* demonstrated the possibility of extracting the interface correlations in the PDF data of an Fe||Fe_3O_4 system using NMF analysis.[24]

In many situations, though, the support structure changes. For a metal on alumina catalysts, interfacial restructuring between the NPs and the Al_2O_3 support is known. Such restructuring of disordered supports often results in a combination of slight shifts of Bragg reflections, slight changes of their line shapes and intensities, and the occurrence of additional phases because of the solid solutions formed at the interfaces. Such complex interfacial restructuring prevents the straightforward calculation of d-PDFs. In some cases, this may result in either the presence of support-related signals in the final data, or an over-subtraction of these signals from the support in the d-PDF, complicating or preventing structural refinements of catalytically active species from d-PDF data.[26]

By applying modulation excitation (ME) conditions in the experiment, richer structural insight into dynamic changes can be gained as demonstrated for infrared (IR) spectroscopy, XAS and XRD experiments.[27–29] A ME experiment is based on modifying a single variable in the system (temperature T, pH, or concentration, in this case, H_2 concentration) and measuring the reaction of the sample to this modulation as a function of time.[30] The modulation could follow different sinusoidal profiles, but for experimental simplicity, usually a square wave profile of the modulation is applied by just opening and closing gas valves in catalytic experiments. The square wave profile can be described by an infinite sum of sinusoidal functions and can undergo the same quantitative and qualitative analysis as a sinusoidal profile.[31]

If the system is reversibly changing during the ME experiment, it is possible to perform a phase-sensitive detection (PSD) analysis of the time-resolved measuring signal.[27,31] The PSD is a mathematical treatment that increases the sensitivity and signal-to-noise ratio of an average response $A(t)$ by converting time-resolved information into phase-sensitive information; see eqn (1):[29,31]

$$A_k\left(\phi_k^{\mathrm{PSD}}\right) = \frac{2}{T}\int_0^T A(t)\sin\left(k\omega t + \phi_k^{\mathrm{PSD}}\right)\mathrm{d}t \qquad (1)$$

where $A_k(\phi_k^{\mathrm{PSD}})$ = species response in the phase domain, $A(t)$ = total response in the time domain, T = length of the period, k = demodulation index, ω = stimulation frequency, and ϕ_k^{PSD} = demodulation phase angle.

It follows from eqn (1) that any spectator species that does not change during the modulation will not contribute to the final response $A_k(\phi^{\mathrm{PSD}})$. All contributions that change randomly without following the modulation also do not contribute to the final response. This means that in the PSD-transformed data, only signals of active species are present. In this way, the signal-to-noise ratio is improved. For more details on the mathematical derivation, see Baurecht *et al.*[29] and for a supportive illustration of the mathematics of the PSD principle as applied to the IR data of heterogeneous catalysts, see Urakawa *et al.*[31]

Here, for the first time to our knowledge, we exploit modulation excitation PDF experiments (ME-PDF) and showcase the increased sensitivity compared to d-PDF analysis for two Ni@Al_2O_3 methanation catalysts with alternating catalysis cycles and full H_2 dropouts. Combining these with the simultaneous monitoring of the catalytic reaction using a mass spectrometer (MS), we obtain information about the involvement of the support in the catalytic process, as well as on the metal–support interactions and the redox dynamics of Ni nanoparticles.

2. Experimental procedure

2a. Catalyst synthesis

The support materials of nominally γ-Al_2O_3 structure called SBa150 were provided by Sasol, Germany. These support materials were used without further purification or treatment for the preparation of Ni@γ-Al_2O_3 catalysts following a urea deposition–precipitation method.[13,32] Briefly, to a 25 mL Ni$(NO_3)_2$ water solution, urea was added under constant stirring at room temperature (molar ratio, urea : Ni = 4 : 1). When a clear green solution was obtained, an Al_2O_3 suspension (1.8 g of Al_2O_3 in 50 mL of ultrapure water) was added and the reaction was performed for 48 h at 90 °C, while constantly stirring. The green precipitate was washed with water and dried over-

 This journal is © The Royal Society of Chemistry 2025

Open Access Article. Published on 10 July 2025. Downloaded on 8/5/2025 7:55:36 PM.
This article is licensed under a Creative Commons Attribution 3.0 Unported Licence.

night in an oven at 90 °C and the resulting powder was calcined at 400 °C for 3 h. The sample (named Ni@SBa150) showed a total amount of Ni of 8.7 ± 0.2 wt% by inductively coupled plasma optical emission spectroscopy (ICP-OES) analysis. An industrially employed catalyst called SPP2080-IMRC, provided by the SPP2080 priority program 'catalysts and reactors under dynamic conditions for energy storage and conversion', funded by the German Research Foundation, was used as a reference due to its similarity in composition to the synthesized one and had a total Ni content of 8.6 wt%.[33]

2b. Modulation excitation (ME) catalytic experiment

5 mg of the sample were placed in a quartz glass capillary with an internal diameter of 1.5 mm (wall thickness: 0.1 mm) and held in place with glass wool. During the activation process, a temperature of 450 °C was reached with a temperature ramp of 10 °C min^{-1} under a pure H_2 atmosphere (a flow rate of 24 mL min^{-1} controlled by Alicat mass flow controllers). Once the temperature was reached, the activation process was performed for 1 h. ME experiment with a square-wave profile was performed by switching between two conditions within one cycle:

- Methanation conditions with a gas composition equal to the stoichiometric ratio of H_2 and CO_2 of 4 : 1 in the methanation reaction. The total flow was 24 mL min^{-1} ($H_2 : CO_2 : He$ = 4 : 1 : 1);
- Full H_2 dropout in which all H_2 was replaced with He for keeping the gas flow constant at 24 mL min^{-1} (*i.e.*, $CO_2 : He$ = 1 : 5).

The two conditions were alternated every 30 minutes for a total of 6 cycles, *i.e.*, 6 methanation and 6 dropout conditions.

The gas outlet of the quartz capillary was connected to a HAS-301-1239A mass spectrometer (MS) (Hiden Analytical QGA), a schematic description of the setup can be found in Fig. S1.† During the experiments, the MS was collecting continuously the mass-to-charge ratio (m/z) in a range from 1 to 100 with a time resolution of 3 seconds. The CO_2 methanation reaction was followed by tracking the signals of the MS at a value of m/z 13 for CH_4 and 44 for CO_2 (Fig. S2†). The selection of the peak at m/z = 13 was made since the molecular peak of CH_4 at m/z = 16 and the peak at m/z = 15 could be influenced by other compounds such as water and oxygen.[34]

2c. Modulated excitation PDF (ME-PDF) experiments

Synchrotron total scattering data were collected at beamline I15-1 at the Diamond Light Source in Didcot, Oxford, UK, with an X-ray energy of 76.69 keV (0.162 Å)with the X-ray beam placed in the corner of the PerkinElmer XRD 4343 CT detector in order to achieve a momentum transfer range of 0.8–25 $Å^{-1}$ with a time resolution of 30 seconds. All experiments were carried out in a quartz capillary reactor (see subsection 2b and Fig. S1†) with heating coils on top and below the capillary. A gas dosing system of Alicat mass flow controllers was used to create the ME conditions. Radial integration of the total scattering data was performed using the software DAWN,[35] PDF calculations were performed using PDFgetX3[36] and PDF modelling was performed using Diffpy-CMI.[37] All the PDF data were processed by using an R_{poly} value equal to 0.9. The instrument parameters Q_{damp} and Q_{broad} were obtained by measuring a LaB_6 standard and resulted in Q_{damp} = 0.0098 $Å^{-1}$ and Q_{broad} = 0.012 $Å^{-1}$. The goodness of fit, R_W, is defined by eqn (2), where $G_{obs}(r)$ and $G_{calc}(r)$ are the observed and calculated PDFs, $w(r_i)$ is the weighting factor of each data point i, and s is the scale factor of the model to the data.[38]

$$R_W = \left\{ \frac{\sum_i w(r_i)[G_{obs}(r_i) - sG_{calc}(r_i)](r_i)^2}{\sum_i w(r_i)[G_{obs}(r_i)]^2} \right\}^{\frac{1}{2}} \quad (2)$$

3. Results and discussion

3a. Catalytic measurements

The catalytic results were obtained for each point in the dataset, and Table 1 shows the average results with the standard deviation.

The conversion of CO_2 (S_{CO_2}) was calculated using eqn (S1) in the ESI,† while the selectivity towards methane formation (Y_{CH_4}) was calculated by following eqn (S2).† The evolution of CH_4 as a function of time is presented in Fig. S2.†

The two catalysts showed similar results. Although the SPP2080-IMRC reference catalyst showed higher CO_2 conversion and selectivity, the results are comparable within errors. It is important to point out that the catalytic experiments were performed in a flow cell built in order to obtain suitable X-ray total scattering data for PDF analysis and, for this reason, the gas hourly space velocity (GHSV) during the *in situ* methanation experiments was 160 000 h^{-1}. This means that the contact time between the gas species and the catalysts was short, but the results are comparable to those reported by Weber *et al.*[33]

3b. Fitting of time-resolved PDF data

In order to access which structural changes of the Ni@Al_2O_3 catalyst can be identified during the dynamic scenario of methanation and dropout conditions, we compared the common biphasic refinements of the time-resolved PDF data in this subsection, with the qualitative interpretation of PSD-transformed ME-PDF data in the next subsection (3c) and with refinements of these PSD-transformed ME-PDF data in the subsection (3d).

First, biphasic refinements of the time-resolved PDF data were performed with a Ni_{fcc} phase and a δ_5-Al_2O_3 phase, which we just recently found to yield the best PDF fits to a range of

Table 1 CO_2 conversion and CH_4 selectivity calculated for the two samples

Sample	%CO_2 conversion	%CH_4 selectivity
SPP2080-IMRC	(57 ± 1)	(74 ± 12)
Ni@SBa150	(54 ± 1)	(72 ± 12)

Open Access Article. Published on 10 July 2025. Downloaded on 8/5/2025 7:55:36 PM.
This article is licensed under a Creative Commons Attribution 3.0 Unported Licence.

PDF datasets of commercial γ-Al_2O_3 supports, such as the SBa150 employed here and the SPP2080-IMRC reference catalyst.[39,40] All PDF data collected are shown in Fig. S3.† All datasets were refined over an r range from 1 to 100 Å. For each phase, the scale value and the lattice parameters were refined first, followed by the isotropic atomic displacement parameter B_{iso} and the parameter δ_2 for the correlated atomic motion of nearest neighbors. Then, the characteristic shape function for spherical nanoparticles was used to fit the domain size of the NPs. For the catalyst samples, we confirmed the good NP dispersion *via* scanning transmission electron microscopy (STEM), showing that our crystallite diameters from PDF analysis align with particle diameters in STEM, see Fig. S6.†

Over an experimental duration of 7.5 hours, for all datasets, the refined scale, lattice parameters and domain size concerning the Al_2O_3 support were constant as expected (see Fig. S5†) and are thus not reported in the table of fit results in the ESI (Table S1†). In contrast, the dynamics in the Ni lattice parameter a and the Ni particle size changed in synchrony with the methanation and dropout cycles; see Fig. 1 and values in Table S1.† The addition of NiO or $NiAl_2O_4$ as additional phases did not improve the refinements.

For the Ni lattice parameter, we observed an increase during the H_2 dropout conditions and a decreases during the methanation scenario for both samples, see Fig. 1a.[41] Herein, the different shapes of the curves are particularly interesting. In the case of SPP2080-IMRC, the value of the lattice parameter a jumps as soon as the dropout starts and jumps back to a low value during the methanation. Such a jump is characteristic for zero-order kinetic processes.[42] In contrast, for Ni@SBa150, the lattice parameters increase during the first two cycles quite strongly and increase more slowly thereafter, following an exponential curve, usually describing a process with first order kinetics.[43,44] In a zero-order process, the kinetics of the process is not affected by the change in the concentration of any of the reactants, *e.g.*, H_2 and Ni^{2+} spices. In a first-order process, the kinetics are influenced by the concentration of a species. Hence, in the case of the Ni@SBa150 sample, NP formation is influenced by the concentration of a reactant, probably a surface species, *e.g.*, surface OH groups from Al_2O_3 or interfacial $NiAl_2O_4$ (not directly detectable from the PDF data), describing an interaction and direct involvement of this species in the methanation process.

The "breathing" behavior was also detected in the Ni particle size, but with an opposite trend to the one found for the lattice parameters. The average NP diameter, in the case of the SPP2080-IMRC catalyst, increases during the methanation and remains approximately constant during the dropout conditions. On the other hand, the NP diameter of the Ni@SBa150 sample increases strongly during the first methanation cycle by almost a nanometer, but then the continued growth due to NP breathing is less pronounced compared to the SPP2080-IMRC sample (see Table S1†). We assume at present that this behaviour results from surface reconstruction which can commonly occur on the surface of transition metal-based catalysts in contact with gases, but detailed studies are still ongoing.[3] These observations for the Ni@SBa150 sample lead to the possibility of an interaction between the nanoparticles and the support which reduces the Ni nanoparticles reflected in the "breathing" in such a dynamic scenario. By analyzing the *in situ* PDF data, though it was not possible to identify any clear structural change associated with the interaction between the Ni NPs and the γ-Al_2O_3 surface.

3c. Qualitative analysis of the phase-resolved ME-PDF data

In order to increase the signal-to-noise ratio of the PDF data and to potentially access interfacial restructuring indicative of the interaction of Ni NPs with the support, we applied the PSD transformation to our ME-PDF datasets. For the PSD transformation, we used an open access python code and applied it to our time-resolved $G(r)$ datasets.[45] The square-wave modulation of the H_2 concentration in between catalysis and dropouts made the dataset suitable for this transformation.[31] To study the first harmonic function, the demodulation factor k

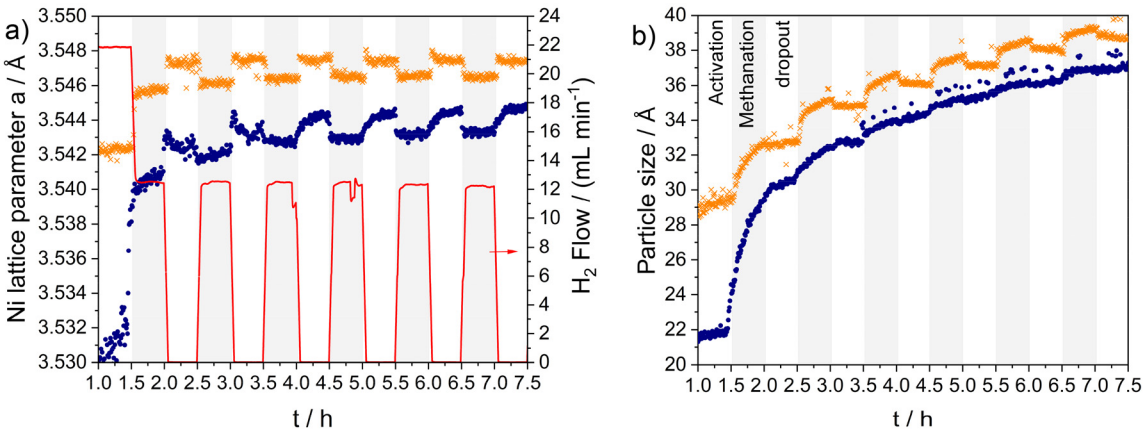

Fig. 1 (a) Evolution of lattice parameters for the Ni@SBa150 (blue circle) and SPP2080-IMRC (orange crosses) catalysts during the experiment. The H_2 flow is presented in red. (b) Evolution of the particle size for the two catalysts during methanation (gray area) and H_2 dropout (white area). The values were obtained by PDF fitting.

 This journal is © The Royal Society of Chemistry 2025

Open Access Article. Published on 10 July 2025. Downloaded on 8/5/2025 7:55:36 PM.
This article is licensed under a Creative Commons Attribution 3.0 Unported Licence.

was set equal to 1 for both samples and the demodulation angle ϕ^{PSD} was changed with a step size of 5° in the 0° < ϕ^{PSD} < 360°range. This operation produces a new set of data, which, in the case of a 5° step size, is made of 72 different $G(r, \phi^{PSD})$ datasets.

The signal intensity of the new phase-resolved dataset shows an oscillating behavior that can be analytically derived from eqn (1) and described in eqn (3).[29,31]

$$G(r, \phi^{PSD}) = A\cos(\varphi - \phi^{PSD}) \quad (3)$$

where φ is the phase delay with respect to the stimulation (phase lag). The intensity of the phase domain data follows the oscillatory behaviour of a cosine function for each r value. Hence, for each single point r, a maximum intensity can be observed for $G_r(\phi^{PSD})$ when $\cos(\varphi - \phi^{PSD}) = 1$. The angle ϕ^{PSD}, at which this condition is fulfilled, is called the in-phase angle and shows the maximum intensity. The angle ϕ at which the intensity is at the minimum is found for $\cos(\varphi - \phi^{PSD}) = -1$ and it is called the anti-phase angle. From this mathematical description, there is also a value of ϕ for which $\cos(\varphi - \phi^{PSD}) = 0$ and the intensity goes to zero, representing the out-of-phase angle. It is important to point out that from this mathematical interpretation, the plot obtained after the PSD transformation is specular around 0.

In Fig. 2a and b, the obtained phase-domain PDF data are shown for both samples. In Fig. 2 panel c and d, the peak intensity associated with the Ni–Ni distance (2.48 Å) is shown as a function of the PSD angle ϕ for both samples. From this, it was possible to find that the in-phase angles are 335° and 0° for Ni@SBa150 and SPP2080-IMRC, respectively.

An important aspect of the PSD analysis is that this mathematical transformation extracts the dynamic changes occurring during the ME experiment. In the case of ME-PDF, the changes observed are related to the formation or disappearance of atomic pairs.

By taking into account the $G(r, \phi$ = in-phase angle), see Fig. 2a and b, it is possible to observe that the Ni_{fcc} peaks are the most intense regardless the low loading. However, we identified additional peaks in the curves of the in-phase angle which is related to a metal–oxygen distance between 1.7 and 2.0 Å with a strong negative intensity. In the case of Ni@SBa150, the peak lies at 1.81 Å, a typical Al–O distance for tetrahedral coordination in the γ-Al_2O_3 structure, while for SPP2080-IMRC, the peak is at 2.00 Å, which can be attributed to the Ni–O distance in the NiO structure. This observation is further illustrated in Fig. 2c, in which the phase angular variation of the distance at 1.81 Å is plotted for Ni@SBa150. The signal of the Al–O peak is the anti-phase compared to the Ni–Ni peak.

From the time-dependent ME-PDF data, we observed an increase in intensity of the Ni–Ni peak at 2.48 Å during the methanation conditions, followed by its decrease during the dropout conditions (Fig. S4†). For this reason, the appearance of strong positive peaks in the phase domain ME-PDF data, related to the Ni NPs, allows us to say that the in-phase angle refers to the methanation conditions, while the anti-phase one is attributed to the full H_2 dropout. From this consideration, it appears that γ-Al_2O_3 undergoes structural changes during the dropout conditions.

The phase domain ME-PDF data for the SPP2080-IMRC sample show two interesting peaks that are not present in the Ni@SBa150 sample. The two peaks are located at 2.00 and 2.97 Å and can be attributed to the Ni–O and Ni–(O)–Ni distances for the NiO structure (see Fig. 2b). These peaks indicate oxidation of the Ni NP surface and hence redox dynamics during the ME experiment, which cannot be identified in the time-dependent data in subsection 3b.

These observations are consistent with, but richer than, what we observed in the time-dependent PDF data. An interaction of the support material with the Ni NPs exists for the Ni@SBa150 sample as identified by Al–O peaks in the PSD-transformed ME-PDF data. This interaction limits the liberty of the Ni NPs to undergo surface reconstruction and sintering. In contrast, for SPP2080-IMRC, the support interaction is less pronounced as Al_2O_3 peaks are not identified in the PSD data, while the Ni NPs undergo oxidation during the dropout conditions as indicated by Ni–O and Ni–(O)–Ni peaks in the ME-PDF data.

3d. Fitting of the phase-resolved ME-PDF data

The data in the phase domain generated by the PSD transformation are more complex to interpret than the normal PDF data collected in the time domain. As explained in subsection 3c, the intensity as a function of the phase angle of each peak follows a cosine function. The maximum amplitude of this cosine function reaches at different phase values ϕ for the Ni and Al_2O_3 contribution. This directly reflects that the maximum amounts of Ni and restructured Al_2O_3 are at different points in time in reference to the starting time of the hydrogen dropouts. Therefore, the PSD-transformed PDF for a certain phase value ϕ consists, for instance, of the maximum positive amplitude of one material phase, *e.g.*, Ni_{fcc} NPs, but additionally features signals from the second material, *e.g.*, Al_2O_3, which are not at their maximum positive or negative amplitude, but somewhere in between. Another important feature is that in the case a structure does not completely disappear during the modulation, as in our case for Ni and Al_2O_3, the PSD-transformed ME-PDF represents only the structural changes happening during the experiment and not the complete structure. From these considerations, the fit of these datasets with crystal structures, as done for the PDF in subsection 3b, can be performed by taking into account the possibility of negative scale values representing the anti-phase structures. Since, as observed in subsection 3b, the most intense peak of the PSD-transformed ME-PDF data belongs to the Ni–Ni distance, a single-phase fit procedure was performed on the in-phase dataset with a Ni_{fcc} structure. For the SPP2080-IMRC catalyst, a good fit quality with an R_W of 0.22 is achieved with the Ni_{fcc} structure (see Fig. 3b), while for the Ni@SBa150 sample, the fit gave an R_W value of 0.62 (see Fig. 3a). For the Ni@SBa150 catalyst prepared *via* deposition–precipitation, we

Open Access Article. Published on 10 July 2025. Downloaded on 8/5/2025 7:55:36 PM.
This article is licensed under a Creative Commons Attribution 3.0 Unported Licence.

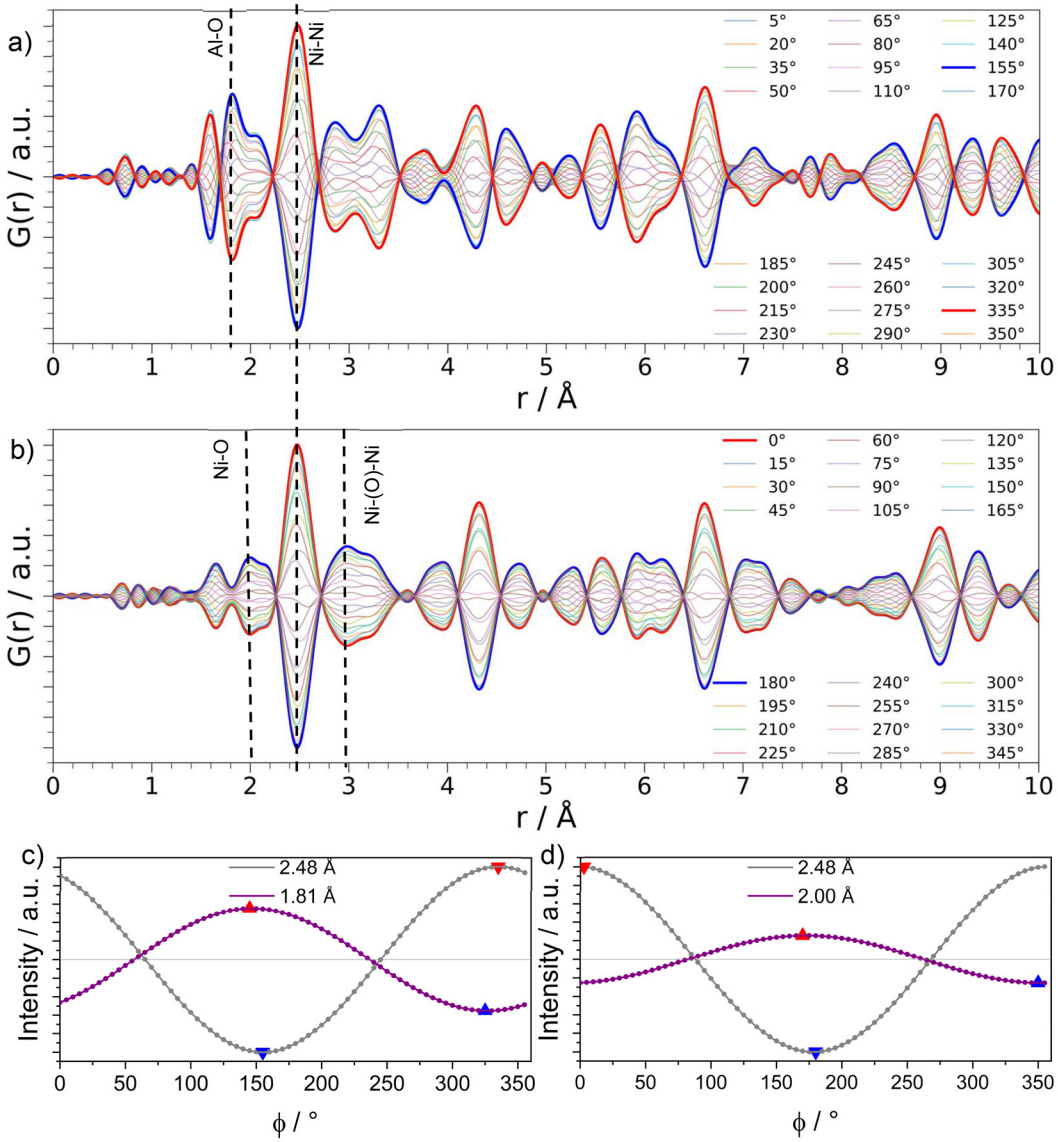

Fig. 2 PSD-transformed data for Ni@SBa150 (a) and SPP2080-IMRC (b). The data are shown for values of the phase ϕ from 0° to 360° with an angular resolution of 15°. The in-phase angle is shown in red (335° for Ni@SBa150 and 0° for SPP2080-IMRC), while the anti-phase angle is shown in blue (155° for Ni@SBa150 and 180° for SPP2080-IMRC). For Ni@SBa150, in (c), the variation of intensity for the peaks at 2.48 Å (Ni–Ni distance in the Ni_{fcc} structure) and 1.81 Å (Al–O distance in the γ-Al_2O_3 structure) is shown as a function of the PSD angle ϕ. For SPP2080-IMRC, in (d), the variation of intensity is shown for the peaks at 2.48 and 2.00 Å, with the latter being attributed to the Ni–O distance in the NiO structure. The red triangles represent the in-phase angles and the blue triangles the anti-phase angles.

already identified strong anti-phase signals of Al–O interatomic distances, as shown in Fig. 2a, which stem from the interaction of the Ni NPs with γ-Al_2O_3. This necessitates a biphasic refinement with alumina as the second phase with a negative scale value. The two-phase fit yielded an R_W value of 0.29, with most of the structural features described (see Fig. 3c). For the reference catalyst, the addition of γ-Al_2O_3 did not improve the fit quality. Since we had identified a clear NiO-related signal in the qualitative interpretation of the data in Fig. 2b, a biphasic fit was tried for SPP2080-IMRC using a Ni phase and a NiO phase (Fig. 3d), which improved the fit slightly.

The resulting fit parameters of the biphasic refinements are summarized in Table 2. From the NiO parameters obtained in the SPP2080-IMRC sample, it was possible to observe that probably oxidation occurred only on the surface and produced a single layer oxide with the dimension similar to the crystal lattice parameters of the NiO cubic structure. Since during the dropout conditions only CO_2 and He were flushing into the catalyst, the oxygen for forming NiO probably comes from the dissociation of CO_2. This mechanism was demonstrated by C. Heine *et al.*, who studied CO_2 adsorption on the Ni(111) surface using ambient-pressure X-ray photoelectron spectroscopy, observing a dissociation process forming CO and NiO.[46]

 This journal is © The Royal Society of Chemistry 2025

Open Access Article. Published on 10 July 2025. Downloaded on 8/5/2025 7:55:36 PM.
This article is licensed under a Creative Commons Attribution 3.0 Unported Licence.

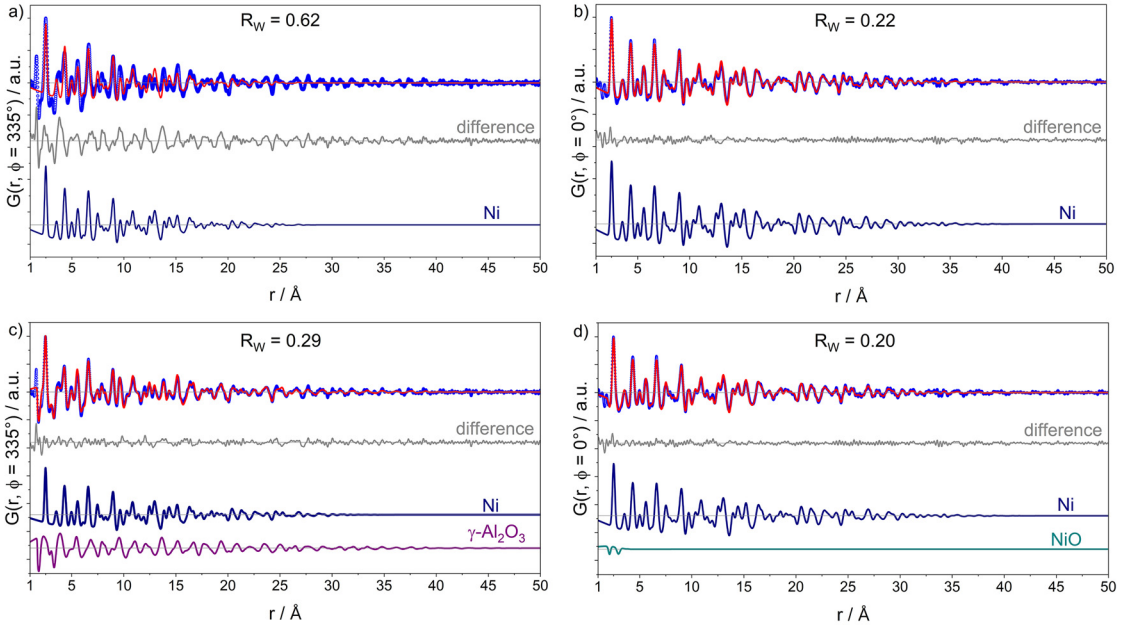

Fig. 3 PDF refinement of the PSD-transformed data for Ni@SBa150 (a and c) and SPP2080-IMRC (b and d). The one-phase refinement was performed with Ni_{fcc} for Ni@SBa150 (a) and SPP2080-IMRC (b). The two-phase refinement was performed with Ni_{fcc} and γ-Al_2O_3 (negative scale) for Ni@SBa150 (c), but with Ni_{fcc} and NiO (negative scale) for SPP2080-IMRC (d). Experimental PDF data are shown as blue circles, the fitted calculated PDF is shown as a red line, and the difference curve is shown in grey (offset), with the goodness-of-fit, R_W, in each panel.

Table 2 PDF fit results for the PSD-transformed data

Parameters	SPP2080-IMRC	Ni@SBa150
Ni *a*/Å	3.538	3.5203
Ni particle size/Å	42.8	36.1
NiO *a*/Å	4.214	—
NiO particle size/Å	4.6	—

In contrast, the absence of detectable surface oxidation of Ni in the Ni@SBa150 sample suggests a different behavior, likely influenced by the Al_2O_3 support. During the dropout conditions, the signals related to Al–O distances increase in intensity and they appear in the PSD transformed data. This suggests that the oxygen previously generated from CO_2 dissociation does not oxidize the Ni nanoparticles, but can interact with the alumina surface. The complex structure of γ-Al_2O_3 may facilitate this interaction, allowing the oxygen to be incorporated into the alumina and contribute to surface reconstruction of the alumina support.

3e. Comparison between PSD-transformed ME-PDF and d-PDF data

So far, in most *in situ* total scattering experiments, insight into the supported species in heterogeneous catalysts is gained *via* refinements of d-PDFs. The identification and main characteristics of the NPs and support phase are captured reasonably well by this approach, also here for the two samples Ni@SBa150 and SPP2080-IMRC. However, the ME-PDF data provide additional insight into subtle and reversible structural changes occurring during the change from catalysis to dropout conditions. In Fig. 4, we compared the d-PDF for t = 1.5 h under methanation conditions (after subtraction of the bare γ-Al_2O_3 support) and the PSD-transformed ME-PDF $G(r, \phi^{PSD} = 0°)$. While in both PDFs, the signals from the Ni structure are the most intense and well observed in all the r space, the d-PDF features high ripples for r < 2 Å and several small ripples such as at 2.0 and 2.8 Å, which are intensified only by

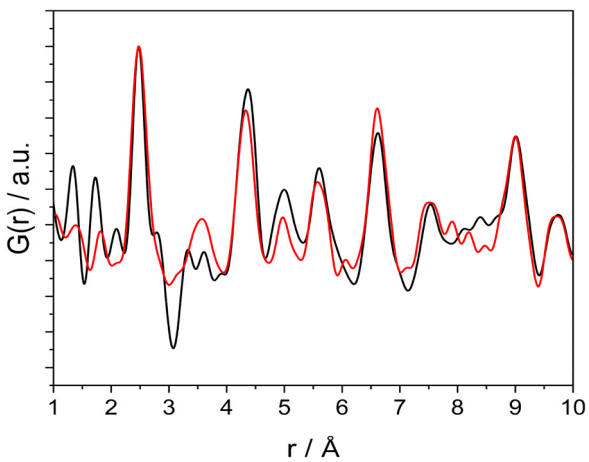

Fig. 4 Comparison between the d-PDF (black) and the PSD transformed ME-PDF data at the in-phase angle ϕ^{PSD} = 0° (in red) for the SPP2080-IMRC sample in the r range between 1 and 10 Å. The d-PDF pattern reported is from the first dataset right after the activation process as soon the methanation starts (t = 1.5 h). The data shown are normalized to the most intense peak (2.48 Å) for better comparison.

Open Access Article. Published on 10 July 2025. Downloaded on 8/5/2025 7:55:36 PM.
This article is licensed under a Creative Commons Attribution 3.0 Unported Licence.

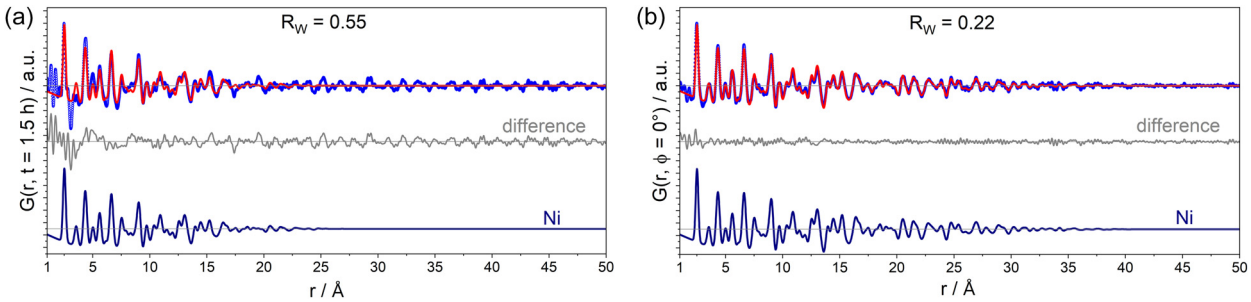

Fig. 5 PDF refinement of d-PDF (a) and PSD data (b) using Ni_{fcc} as a single phase. Experimental PDF data are shown as blue circles, the fitted calculated PDF is shown as a red line, and the difference curve is shown in grey (offset), with the goodness-of-fit, R_W, in each panel.

the subtraction of γ-Al_2O_3. Moreover, the peak in the PSD data at 3.55 Å, which is related to interatomic distances of the second coordination shell in the Ni_{fcc} structure, splits into two unphysically small peaks in the d-PDF data. Another important difference is the negative peak at 3.0 Å in the d-PDF plot, indicating the introduction of errors in the subtraction. These differences clearly show the superior signal-to-noise ratio of the ME-PDF data, enabling a better fit quality compared to the d-PDF.

To demonstrate the power of PSD analysis and the better signal-to-noise ratio of PSD-derived ME-PDF datasets, we fitted both the d-PDF and the PSD-transformed ME-PDF data with a Ni_{fcc} structure each; see Fig. 5. The high noise and structural remnants of the Al_2O_3 support in the d-PDF data result in a low quality of fit with R_W = 0.55 and an underestimation of the particle diameter because of dominating noise for r values larger than about 25 Å. In contrast, the ME-PDF accesses the NP diameter more reliably with less noise over the entire r range, with a significantly less noisy difference curve and a better R_W value of 0.22.

This comparison thus shows the advantages of PSD analysis of ME-PDF datasets for the structural characterization of samples with complex and structurally changing support materials like γ-Al_2O_3 under operating conditions. PSD analysis overcomes the need for d-PDF analysis for the subtraction of an unloaded reference material, but isolates the signals from the time-dependent measurements with the improved signal-to-noise being more sensitive to subtle changes.

4. Conclusion

In this work, we have shown that phase-sensitive detection (PSD) analysis can be successfully applied to modulation excitation pair distribution function (ME-PDF) data. Two catalysts prepared *via* different synthesis routes were compared, and although their activity and selectivity were comparable, they behaved differently from a structural point of view under methanation and dropout conditions. From regular PDF analysis with biphasic refinements employing a Ni_{fcc} phase and an alumina phase, the SPP2080-IMRC and Ni@SBa150 catalysts showed some oscillatory trends of lattice parameters and particle size as a function of methanation and dropout conditions. The nature of the jumps in lattice parameters when switching from methanation to dropout conditions points towards an interaction between the nanoparticles and the support for the Ni@SBa150 catalyst prepared *via* deposition–precipitation.

In order to deepen the structural insight and improve the signal-to-noise ratio of the PDF data, we applied the PSD transformation to the time-dependent ME-PDF data. These phase-resolved ME-PDF data then revealed additional structural differences between the two catalysts.

First, the assumed nanoparticle–support interaction in the Ni@SBa150 catalyst was consolidated, since γ-Al_2O_3 signals were present in the phase-resolved data, indicating structural reorganization of the support in the catalytic and dropout process. From the analysis of the intensity of phase-resolved PDFs as a function of phase angle, the structural changes in the support were shown to be in the anti-phase with the changes in the Ni nanoparticles, with the latter being involved in the methanation scenario and the support under the dropout conditions. Second, for the SPP2080-IMRC sample, an interatomic distance was clearly identified at 2.97 Å only in the PSD data. This peak belongs to the Ni–(O)–Ni distance in the NiO structure stemming from surface oxidation of the Ni NPs during hydrogen dropouts, and it was completely invisible in the time-dependent PDF data because of its low amount.

Hence, for both samples, the improved signal-to-noise ratio of phase-resolved PDFs yielded additional insight into the nanoparticle–support interaction and surface redox processes, both of which were not identified in the regular PDF data.

The PSD data showed us how the synthetic route can impact the structural response of a catalyst over the six methanation–dropout cycles investigated despite similar catalytic performance. For the Ni@SBa150 sample prepared *via* deposition–precipitation, γ-Al_2O_3 is not an inert spectator but experiences interfacial restructuring during catalytic cycling, with further studies ongoing as to the structural mechanism. The dynamic restructuring of the γ-Al_2O_3 support supposedly helps in keeping the active Ni nanoparticles stable and preventing their oxidation as opposed to the SPP2080-IMRC catalyst, in which the Ni nanoparticles oxidize during the dropouts, while the support structure is unaffected by the reaction

 This journal is © The Royal Society of Chemistry 2025

Open Access Article. Published on 10 July 2025. Downloaded on 8/5/2025 7:55:36 PM.
This article is licensed under a Creative Commons Attribution 3.0 Unported Licence.

conditions. To conclude, ME-PDF experiments present a powerful tool to provide additional insight into the structure–property relationships of heterogeneous catalysts, opening a huge opportunity for studying disordered materials under working conditions.

Conflicts of interest

There are no conflicts of interest to declare.

Data availability

The data analysed for this article are available in a public GitHub repository at **https://github.com/Fabio1911/MEPDF_data.git**.

Acknowledgements

We acknowledge funding by the Deutsche Forschungsgemeinschaft (DFG, German Research Foundation) *via* SPP2080 (ZO 369/2-2) and grant no. 441718867. We acknowledge the beamtime at beamline I15-1 at the Diamond Light Source (Didcot, UK), proposal CY34358-2. We thank Hitachi High-Technology for providing the STEM capabilities. We gratefully acknowledge Anna Herlihy and Philip Chater (I15-1) for support during the beamtime, as well as our colleagues Hannah Fink, Anna Wächtler and Felix Egger for helping in the data acquisition and Lars Peters for proofreading.

References

1 K. M. Neyman and S. M. Kozlov, Quantifying interactions on interfaces between metal particles and oxide supports in catalytic nanomaterials, *NPG Asia Mater.*, 2022, **14**, 59, DOI: **10.1038/s41427-022-00405-4**.

2 C. Mager-Maury, G. Bonnard, C. Chizallet, P. Sautet and P. Raybaud, H_2 -Induced Reconstruction of Supported Pt Clusters: Metal-Support Interaction versus Surface Hydride, *ChemCatChem*, 2011, **3**, 200–207.

3 R. A. van Santen, in *Modern Heterogeneous Catalysis*, John Wiley & Sons, Ltd, 2017, pp. 117–143.

4 M. A. van Hove, R. J. Koestner, P. C. Stair, J. P. Bibérian, L. L. Kesmodel, I. Bartoš and G. A. Somorjai, The surface reconstructions of the (100) crystal faces of iridium, platinum and gold, *Surf. Sci.*, 1981, **103**, 189–217.

5 J. E. Demuth, The Crystallography of Clean Surfaces and Chemisorbed Species as Determined by Low-Energy Electron Diffraction, *J. Colloid Interface Sci.*, 1977, 184–197.

6 M. Monai, K. Jenkinson, A. E. M. Melcherts, J. N. Louwen, E. A. Irmak, S. Van Aert, T. Altantzis, C. Vogt, W. van der Stam, T. Duchoň, B. Šmíd, E. Groeneveld, P. Berben, S. Bals and B. M. Weckhuysen, Restructuring of titanium oxide overlayers over nickel nanoparticles during catalysis, *Science*, 2023, **380**, 644–651.

7 G. Garbarino, P. Riani, A. Infantes-Molina, E. Rodríguez-Castellón and G. Busca, On the detectability limits of nickel species on NiO/γ-Al 2 O 3 catalytic materials, *Appl. Catal., A*, 2016, **525**, 180–189.

8 A. Parastaev, V. Muravev, E. H. Osta, T. F. Kimpel, J. F. M. Simons, A. J. F. van Hoof, E. Uslamin, L. Zhang, J. J. C. Struijs, D. B. Burueva, E. V. Pokochueva, K. V. Kovtunov, I. V. Koptyug, I. J. Villar-Garcia, C. Escudero, T. Altantzis, P. Liu, A. Béché, S. Bals, N. Kosinov and E. J. M. Hensen, Breaking structure sensitivity in CO2 hydrogenation by tuning metal-oxide interfaces in supported cobalt nanoparticles, *Nat. Catal.*, 2022, **5**, 1051–1060.

9 C. Vogt, E. Groeneveld, G. Kamsma, M. Nachtegaal, L. Lu, C. J. Kiely, P. H. Berben, F. Meirer and B. M. Weckhuysen, Unravelling structure sensitivity in CO2 hydrogenation over nickel, *Nat. Catal.*, 2018, **1**, 127–134.

10 F. Loviat, I. Czekaj, J. Wambach and A. Wokaun, Nickel deposition on γ-Al_2O_3 model catalysts: An experimental and theoretical investigation, *Surf. Sci.*, 2009, **603**, 2210–2217.

11 P. Strucks, L. Failing and S. Kaluza, A Short Review on Ni-Catalyzed Methanation of CO 2 : Reaction Mechanism, Catalyst Deactivation, Dynamic Operation, *Chem. Ing. Tech.*, 2021, **93**, 1526–1536.

12 G. Busca, E. Spennati, P. Riani and G. Garbarino, Looking for an Optimal Composition of Nickel-Based Catalysts for CO2 Methanation, *Energies*, 2023, **16**, 5304.

13 B. Mutz, A. Gänzler, M. Nachtegaal, O. Müller, R. Frahm, W. Kleist and J.-D. Grunwaldt, Surface Oxidation of Supported Ni Particles and Its Impact on the Catalytic Performance during Dynamically Operated Methanation of CO2, *Catalysts*, 2017, **7**, 279.

14 A. Martorana, G. Deganello, A. Longo, F. Deganello, L. Liotta, A. Macaluso, G. Pantaleo, A. Balerna, C. Meneghini and S. Mobilio, Time-resolved X-ray powder diffraction on a three-way catalyst at the GILDA beamline, *J. Synchrotron Radiat.*, 2003, **10**, 177–182.

15 E. Tusini, M. Casapu, A. Zimina, D. E. Doronkin, H. Störmer, L. Barthe, S. Belin and J.-D. Grunwaldt, Structural Changes of Ni and Ni-Pt Methane Steam Reforming Catalysts During Activation, Reaction, and Deactivation Under Dynamic Reaction Conditions, *ACS Catal.*, 2024, **14**, 7463–7477.

16 N. K. Zimmerli, C. R. Müller and P. M. Abdala, Deciphering the structure of heterogeneous catalysts across scales using pair distribution function analysis, *Trends Chem.*, 2022, **4**, 807–821.

17 N. K. Zimmerli, L. Rochlitz, S. Checchia, C. R. Müller, C. Copéret and P. M. Abdala, Structure and Role of a Ga-Promoter in Ni-Based Catalysts for the Selective Hydrogenation of CO2 to Methanol, *JACS Au*, 2024, **4**, 237–252.

Open Access Article. Published on 10 July 2025. Downloaded on 8/5/2025 7:55:36 PM.
This article is licensed under a Creative Commons Attribution 3.0 Unported Licence.

18 G. B. M. Vaughan, R. Baker, R. Barret, J. Bonnefoy, T. Buslaps, S. Checchia, D. Duran, F. Fihman, P. Got, J. Kieffer, S. A. J. Kimber, K. Martel, C. Morawe, D. Mottin, E. Papillon, S. Petitdemange, A. Vamvakeros, J. P. Vieux and M. Di Michiel, ID15A at the ESRF - a beamline for high speed operando X-ray diffraction, diffraction tomography and total scattering, *J. Synchrotron Radiat.*, 2020, **27**, 515–528.

19 S. J. L. Billinge and M. G. Kanatzidis, Beyond crystallography: the study of disorder, nanocrystallinity and crystallographically challenged materials with pair distribution functions, *Chem. Commun.*, 2004, 749–760.

20 M. Zobel, R. B. Neder and S. A. J. Kimber, Universal solvent restructuring induced by colloidal nanoparticles, *Science*, 2015, **347**, 292–294.

21 A. E. Platero-Prats, Z. Li, L. C. Gallington, A. W. Peters, J. T. Hupp, O. K. Farha and K. W. Chapman, Addressing the characterisation challenge to understand catalysis in MOFs: the case of nanoscale Cu supported in NU-1000, *Faraday Discuss.*, 2017, **201**, 337–350.

22 S. L. J. Thomä, J. Neuefeind, T. G. A. Youngs and M. Zobel, A strategy of consistent X-ray and neutron double-difference pair distribution function analysis of nanoparticle dispersions, *Colloid Polym. Sci.*, 2024, DOI: **10.1007/s00396-024-05333-z**.

23 T. Qin, L. Li, X. Mu, X. Liu and L. Chen, Structural Evolution of Supported Pt Atoms during Calcination Using Electron Atomic Pair Distribution Function: Implications for Catalysis, *ACS Appl. Nano Mater.*, 2024, **7**, 20474–20483.

24 H. S. Geddes, H. D. Hutchinson, A. R. Ha, N. P. Funnell and A. L. Goodwin, Extracting interface correlations from the pair distribution function of composite materials, *Nanoscale*, 2021, **13**, 13220–13224.

25 K. W. Chapman, S. H. Lapidus and P. J. Chupas, Applications of principal component analysis to pair distribution function data, *J. Appl. Crystallogr.*, 2015, **48**, 1619–1626.

26 S. Schlicher, N. Prinz, J. Bürger, A. Omlor, C. Singer, M. Zobel, R. Schoch, J. K. N. Lindner, V. Schünemann, S. Kureti and M. Bauer, Quality or Quantity? How Structural Parameters Affect Catalytic Activity of Iron Oxides for CO Oxidation, *Catalysts*, 2022, **12**, 675.

27 D. Ferri, M. A. Newton, M. Di Michiel, G. L. Chiarello, S. Yoon, Y. Lu and J. Andrieux, Revealing the Dynamic Structure of Complex Solid Catalysts Using Modulated Excitation X-ray Diffraction, *Angew. Chem.*, 2014, **126**, 9036–9040.

28 G. L. Chiarello and D. Ferri, Modulated excitation extended X-ray absorption fine structure spectroscopy, *Phys. Chem. Chem. Phys.*, 2015, **17**, 10579–10591.

29 D. Baurecht and U. P. Fringeli, Quantitative modulated excitation Fourier transform infrared spectroscopy, *Rev. Sci. Instrum.*, 2001, **72**, 3782–3792.

30 P. Müller and I. Hermans, Applications of Modulation Excitation Spectroscopy in Heterogeneous Catalysis, *Ind. Eng. Chem. Res.*, 2017, **56**, 1123–1136.

31 A. Urakawa, T. Bürgi and A. Baiker, Sensitivity enhancement and dynamic behavior analysis by modulation excitation spectroscopy: Principle and application in heterogeneous catalysis, *Chem. Eng. Sci.*, 2008, **63**, 4902–4909.

32 K. P. de Jong, *Synthesis of Solid Catalysts*, John Wiley & Sons, Ltd, 2009, pp. 111–134.

33 S. Weber, R. T. Zimmermann, J. Bremer, K. L. Abel, D. Poppitz, N. Prinz, J. Ilsemann, S. Wendholt, Q. Yang, R. Pashminehazar, F. Monaco, P. Cloetens, X. Huang, C. Kübel, E. Kondratenko, M. Bauer, M. Bäumer, M. Zobel, R. Gläser, K. Sundmacher and T. L. Sheppard, Digitization in Catalysis Research: Towards a Holistic Description of a Ni/Al_2O_3 Reference Catalyst for CO2 Methanation, *ChemCatChem*, 2022, **14**, e202101878.

34 M. S. Brennwald, Y. Tomonaga and R. Kipfer, Deconvolution and compensation of mass spectrometric overlap interferences with the miniRUEDI portable mass spectrometer, *MethodsX*, 2020, **7**, 101038.

35 M. Basham, J. Filik, M. T. Wharmby, P. C. Y. Chang, B. El Kassaby, M. Gerring, J. Aishima, K. Levik, B. C. A. Pulford, I. Sikharulidze, D. Sneddon, M. Webber, S. S. Dhesi, F. Maccherozzi, O. Svensson, S. Brockhauser, G. Náray and A. W. Ashton, Data Analysis WorkbeNch (DAWN), *J. Synchrotron Radiat.*, 2015, **22**, 853–858.

36 P. Juhás, T. Davis, C. L. Farrow and S. J. L. Billinge, PDFgetX3 : a rapid and highly automatable program for processing powder diffraction data into total scattering pair distribution functions, *J. Appl. Crystallogr.*, 2013, **46**, 560–566.

37 P. Juhás, C. L. Farrow, X. Yang, K. R. Knox and S. J. L. Billinge, Complex modeling: a strategy and software program for combining multiple information sources to solve ill-posed structure and nanostructure inverse problems, *Acta Crystallogr., Sect. A:Found. Adv.*, 2015, **71**, 562–568.

38 P. F. Peterson, E. S. Božin, T. Proffen and S. J. L. Billinge, Improved measures of quality for the atomic pair distribution function, *J. Appl. Crystallogr.*, 2003, **36**, 53–64.

39 F. Manzoni, B. M. D. Fahl and M. Zobel, Improved Structural Description of Different 5-Al_2O_3 Phase via X-ray Pair Distribution Function Analysis, *Catalysts*, 2024, **14**, 238, DOI: **10.3390/catal14040238**.

40 L. Kovarik, M. Bowden, A. Genc, J. Szanyi, C. H. F. Peden and J. H. Kwak, Structure of δ-Alumina: Toward the Atomic Level Understanding of Transition Alumina Phases, *J. Phys. Chem. C*, 2014, **118**, 18051–18058.

41 V. Petkov, S. Shan, P. Chupas, J. Yin, L. Yang, J. Luo and C.-J. Zhong, Noble-transition metal nanoparticle breathing in a reactive gas atmosphere, *Nanoscale*, 2013, **5**, 7379–7387.

42 P. J. Chupas, K. W. Chapman, G. Jennings, P. L. Lee and C. P. Grey, Watching nanoparticles grow: the mechanism and kinetics for the formation of TiO2-supported platinum nanoparticles, *J. Am. Chem. Soc.*, 2007, **129**, 13822–13824.

43 M. A. Newton, S. G. Fiddy, G. Guilera, B. Jyoti and J. Evans, Oxidation/reduction kinetics of supported Rh/Rh_2O3 nano-

 This journal is © The Royal Society of Chemistry 2025

particles in plug flow conditions using dispersive EXAFS, *Chem. Commun.*, 2005, 118–120.
44 P. W. Atkins, J. De Paula and J. H. Keeler, in *Atkins' physical chemistry*, Oxford University Press, Oxford, 11th edn, 2018.
45 J. Weyel, in *Phase Sensitive Detection for Spectroscopy*, Zenodo, 2020.
46 C. Heine, B. A. J. Lechner, H. Bluhm and M. Salmeron, Recycling of CO2: Probing the Chemical State of the Ni(111) Surface during the Methanation Reaction with Ambient-Pressure X-Ray Photoelectron Spectroscopy, *J. Am. Chem. Soc.*, 2016, **138**, 13246–13252.

Open Access Article. Published on 10 July 2025. Downloaded on 8/5/2025 7:55:36 PM.
This article is licensed under a Creative Commons Attribution 3.0 Unported Licence.